Simulation and analysis of pseudo-passive power battery thermal runaway propagation inhibition system

Zhantang Lin[a, b, c] Zeyu Li[a, b, c*] Jiayan Chen[a, b, c] Junrui Deng[a, b, c] Hongwei Wu[d]

[a] *School of Electric Power, South China University of Technology, Guangzhou 510640, China*

[b] *Guangdong Province Key Laboratory of High Efficient and Clean Energy Utilization, South China University of Technology, Guangzhou 510640, China*

[c] *Guangdong Province Engineering Research Center of High Efficient and Low pollution Energy Conversion, Guangzhou 510640, China*

[d] *School of Physics, Engineering and Computer Science, University of Hertfordshire, Hatfield, AL10 9AB, UK*

*Corresponding author. *E-mail address*: epzeyuli@scut.edu.cn

Abstract

Passive power battery thermal runaway propagation inhibition technologies, being able to block the thermal runaway without external power sources, are highly important for the safety of electric vehicles and have attracted extensive attention. The existing passive thermal runaway propagation inhibition approach is based on thermal insulation, leading to the large thermal resistance between batteries and incompatibility with thermal management. In this regard, the pseudo-passive power battery thermal runaway propagation inhibition system, integrating with pseudo-passive heat removal and thermal insulation, is proposed to address the above-mentioned issue. The system model, based on the lumped parameter model of pseudo-passive heat removal and the 3D model of thermal runaway propagation, is developed and verified. A good agreement of the simulation and experiment data is shown, i.e., the average deviation is 6.91%. Furthermore, the system performance is assessed and compared with the existing passive approach. Results display that the pseudo-passive heat removal process addresses 24.6% of the heat generation of the battery array, and the thermal resistance necessary to stop the thermal runaway propagation comes down by 48-85%. The paper provides new insight into power battery thermal runaway propagation inhibition technologies, and is favorable to enhance the safety of electric vehicles.

Keywords

Electric vehicle; Battery safety; Thermal runaway propagation; Pump-driven cooling; Pseudo-passive

Nomenclature		*Greek symbols*	
		α	Seebeck coefficient (V/K), ratio (-)
Symbols		δ	thickness (mm)
A	area (m^2), pre-exponential factor (-)	Δ	difference (-)
C	heat capacity [J/(kg·K)], capacity of battery (Ah)	ε	emissivity (-)
Const	constant (-)	η	efficiency (-)
E	activation energy (J/mol)	λ	thermal conductivity [W/(m·K)], heat flux (W/m^2)
H	heat (J)	ρ	density (kg/m^3)
h	heat transfer coefficient [W/(m^2·K)]	σ	Stefan–Boltzmann constant [W/(m^2·K^4)]
I	current (A)		
k	thermal conductivity [W/(m·K)]	*Subscripts*	
L	specific heat capacity (kJ/kg)	a	activation
m	mass flow (g/s)	Bat	battery
P	power (W)	b	back
p	pressure (Pa)	C	cold junction
Q	heat transfer rate (W)	f	front
q	volume flow (L/min), mass flow (kg/min), heating power (W/m^3)	H	hot junction
R	gas constant (-), resistance (Ω), thermal resistance [W/(m^2·K)]	JR	jelly roll
r	thermophysical parameters (-)	m	mass, logarithmic mean temperature difference
T	temperature (°C)	PCC	phase change composite material
t	time (s)	PCM	phase change material
u	normalized concentration (-)	p	pump
V	volume (m^3)	r	rated
v	flow rate (m/s)	rem	heat removal of pump-driven cooling
x	quality (-)	TE	thermoelectric
		TR	thermal runaway
		t	terminal difference
		v	volume

1. Introduction

The international community widely acknowledges and collectively promotes the development of electric vehicles. Research reveals that global electric vehicle sales approached 14 million in 2023, which is increased by 3.5 million compared to 2022 and emerges a 35% year-on-year growth [1]. As the cornerstone of electric vehicles, lithium-ion batteries are progressively evolving towards higher energy density [2]. However, this advancement frequently brings about safety challenges that impede further progress. A primary safety challenge is thermal runaway propagation, i.e., the thermal runaway propagates from one cell to the neighboring cell by means of thermal abuse. In recent years, incidents of electric vehicle spontaneous combustion led by thermal runaway propagation have become increasingly frequent [3-5], i.e., the fire incidence rate exceeds 0.03%. Consequently, addressing thermal runaway propagation in lithium-ion batteries has become an urgent and critical issue.

Battery thermal runaway propagation inhibition methods can be categorized into cell-level and system-level measures. Cell-level approaches are to enhance the thermostability of the single battery. They are typically based on electrode optimization designs [6] and electrolyte optimization designs [7, 8], such as modifications to the cathode material [9, 10], anode material modifications [11], and electrolyte alterations. However, these often result in a decline in battery performance [12] and usually only serve to delay the thermal runaway propagation. In this regard, system-level methods can effectively achieve thermal runaway propagation inhibition. One of the primary system-level thermal runaway propagation inhibition approaches is by thermal insulation, e.g., supplementing materials with fire-retardancy and low thermal conductivity between batteries to reduce the heat transfer of batteries. The common thermal insulation schemes are shown in Table 1. These schemes can be categorized into three types: inorganic materials, phase change materials (PCMs), and composite phase change materials (PCCs). Inorganic materials usually comprise of metal plates, asbestos, graphite composite sheets, and aerogel. Metal plates are used to enhance heat dissipation, but typically require significant thickness to inhibit the thermal runaway propagation. Asbestos can inhibit the thermal runaway propagation at a small thickness, but it poses health risks and environmental hazards. Graphite composite sheets can inhibit the thermal runaway propagation at moderate thicknesses, but they carry risks of electrical conductivity and high-temperature oxidation. Aerogel layers can only delay the process even at large thicknesses. PCMs are usually difficult to cut off the thermal runaway propagation when it is employed solely. In particular, if paraffin is employed for thermal runaway propagation inhibition, it must be wrapped by fire-retardant materials to avoid combusting itself [23]. Although PCCs effectively inhibit thermal runaway propagation by incorporating additional materials into PCMs, they often entail intricate and demanding manufacturing processes. While effective at inhibiting thermal runaway propagation, these methods also introduce relatively large thermal resistance between batteries. For instance, using 1 mm of asbestos to inhibit thermal runaway propagation in a 27 Ah prismatic lithium-ion battery results in a thermal resistance of 0.0125 ($m^2 \cdot K$)/W [13], which imposes a substantial burden on the daily thermal management of the battery array [24].

Table 1

Thermal insulation based thermal runaway propagation inhibition schemes.

No.	Scheme	Value	Performance
1 [13]	Asbestos layer	δ =1 mm	Inhibition
		λ =0.08 W/(m·K)	
2 [14]	Asbestos layer	δ =1 mm	Inhibition
		λ =0.07-0.1 W/(m·K)	
3 [15]	Graphite composite sheet	δ =2.1 mm	Inhibition
		λ =0.024 W/(m·K)	
4 [16]	Aluminum plate	δ =0.8 mm	Delay
		δ =3.2 mm	Inhibition
		λ =5.0 W/(m·K)	
5 [17]	Copper plate or	δ =0.8 mm	Delay
	aluminum plate	δ =1.6 mm	Delay
		δ =3.2 mm	Inhibition
6 [18]	PCM of silica aerogel	δ =1 mm	Delay
		λ =0.02 W/(m·K)	
7 [19]	Aerogel layer;	δ_1 =3 mm	Delay
		λ_1 =0.0287 W/(m·K)	
	PCM of paraffin;	L_2=124.9 kJ/kg	Accelerate
		λ_2 =0.108 W/(m·K)	
	PCM with expandable graphite	λ_3 =0.2079 W/(m·K)	Delay
		L_3=131.8 kJ/kg	
8 [20]	PCM/graphite composite.	λ =16.6 W/(m·K)	Inhibition
		L =123 kJ/kg	

9 [21]	PCC of wax and graphite	δ =2 mm λ =22.0 W/(m·K) L =165 J/g	Inhibition
10 [22]	PCC of paraffin and silica aerogel	δ =3 mm λ =0.051-0.066 W/(m·K) L =79.24 kJ/kg	Inhibition

Another approach of thermal runaway propagation inhibition is based on heat removal, i.e., employing the heat dissipation unit to cool down the battery, and the recent progress is shown in Table 2. These approaches can be classified into three categories: air cooling, liquid cooling, and a combination of liquid cooling with thermal insulation. Air cooling can only delay the thermal runaway propagation, owing to the poor heat transfer coefficient. The liquid cooling plates with microchannels between the batteries can inhibit the thermal runaway propagation, but they come with high pump power consumption and occupy valuable space within the battery array. It is derived that the integration with thermal insulation and liquid cooling is not only effective in cutting off the thermal runaway propagation but also mitigates the dependence on thermal insulation. For instance, in inhibiting thermal runaway propagation in a series of 37 Ah prismatic lithium-ion batteries, the liquid cooling unit with a heat transfer coefficient of 140 W/(m^2·K) can lower the thermal resistance of aerogel thermal insulation layer to 0.0103 m^2/(K·W). Higher heat transfer coefficients further reduce thermal resistance [33]. The development trend for hybrid solutions is to not only reduce the thermal resistance between batteries necessary to stop the thermal runaway propagation, e.g., through heat transfer enhancement of heat removal unit as well as material modification of thermal insulation, but also extend the applicability in special scenario such as no external power source input to heat removal units.

Table 2

Heat removal based thermal runaway propagation inhibition schemes.

No.	Scheme	Value	Performance
1 [20]	Air flow	h=20 W/(m^2·K)	Delay
2 [25]	Liquid cooling plates between batteries	q_v=30 L/min	Control temperature at 75 °C in 30 s
3 [26]	Aluminum mini-channel cooling system	q_v=10 L/min	Inhibition

4 [27]	Two aluminum plates with mini-channels	v =0.3 m/s	Inhibition
5 [18]	Liquid cooling plate; PCM with liquid cooling plate	q_v=7.8 L/min λ_{PCM} =0.2 W/(m·K)	Delay Inhibition
6 [28]	PCM with liquid cooling plate	v =0.05 m/s λ_{PCM} =0.8 W/(m·K)	Inhibition
7 [29]	PCM with liquid cooling plate on the lateral	q_m=0.12 kg/min L=1920 kJ/kg	Inhibition
8 [30]	PCM with liquid cooling and phase change cooling	v =0.596 m/s h=20 W/(m^2·K) L=225 kJ/kg	Inhibition
9 [31]	PCM with micro-channel cooling plate	q_v=3.9 L/min L=123 kJ/kg	Inhibition
10 [32]	PCC with nanofluids cooling plate	v =0.04 m/s L=225 kJ/kg	Inhibition

Although hybrid solutions integrated with thermal insulation and heat removal can effectively inhibit thermal runaway propagation under conditions of lower thermal resistance, heat removal schemes are active and lead to hybrid solutions failing to work when external power is unavailable. Actually, the response of thermal runaway propagation inhibition in the null input of external energy is highly important. On one hand, 41% of thermal runaway propagation accidents happen at rest conditions [34], when the battery is in a shutdown state. On the other hand, the output voltage of the battery rapidly drops to zero after thermal runaway [35]. Consequently, it is necessary to develop the hybrid thermal runaway propagation inhibition technology which is able to operate without the dependence of external power.

Motivated by the above-mentioned research gaps, the pseudo-passive power battery thermal runaway propagation inhibition system is proposed to stop the thermal runaway propagation in the case of null external power as well as low thermal resistance. The remainder of the paper is organized as follows. In Section 2, the configuration and operation of the system are introduced. In Section 3, a 3D model for thermal runaway propagation in batteries, a 1D model for pump-driven cooling processes, and a model for thermoelectric conversion processes were constructed, and their integrated operation was achieved. In Section 4, the operation of the proposed system is showcased and analyzed. A summary of the study and the conclusions are provided in Section 5. The novelty of this paper lies in the proposal, modeling, and performance evaluation of a pseudo-passive power battery thermal runaway propagation inhibition system. The paper is beneficial for the safety improvement of electric vehicles.

2. System description

The configuration and operation of the system are outlined as follows.

2.1. System configuration

Fig. 1 illustrates the pseudo-passive thermal runaway propagation inhibition system (For clarity of presentation, the components have been appropriately). This system consists of three main parts: (1) the battery array with thermal insulation layers between batteries; (2) the pump-driven cooling unit, serving as the primary heat removal approach; and (3) the thermoelectric module, serving as the power source of the liquid pump and fans as well as the secondary heat removal. The battery array is composed of several cells, and the bottom and side are closely connected with the evaporator and thermoelectric module, respectively. The pump-driven cooling system includes a liquid pump, reservoir, condenser, and evaporator. Water is used as the working fluid, with the evaporator flow channel arranged in a serpentine pattern. Bismuth telluride (Bi_2Te_3) is used as the thermoelectric material, capable of reliable operation under conditions below 330 °C, meeting the operational requirements of the thermal runaway propagation inhibition system.

The primary characteristics of the proposed system lie in the pseudo-passive approach, which totally differs from passive and active methods. Passive systems are independent of power sources, and usually by thermal insulation between batteries. Active systems, on the other hand, usually heat removal units relying on external energy sources, such as liquid cooling systems. The pseudo-passive approach, however, requires energy, but this energy is provided internally instead of externally, e.g., from the heat generation of batteries and known as internal power sources. Obviously, the proposed pseudo-passive system has the similar applicability to the passive one, and is capable of operating reliably in the case of null external power source input.

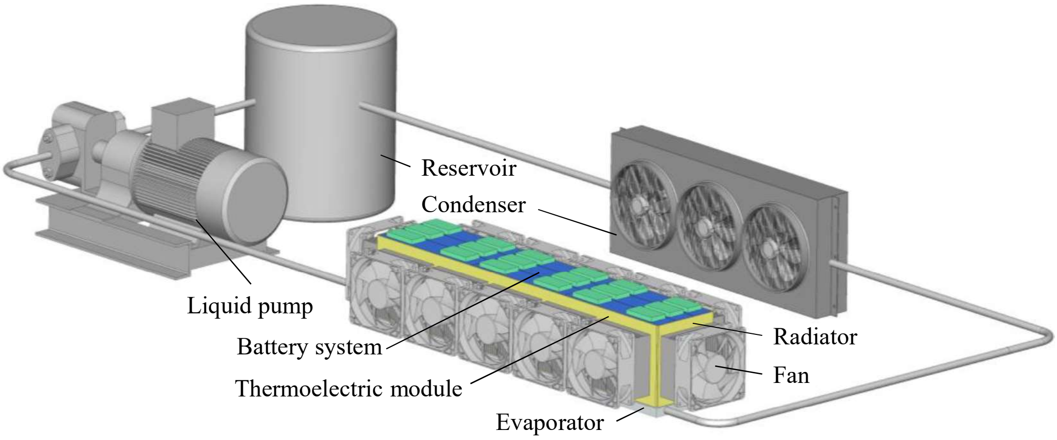

Fig. 1. Pseudo-passive power battery thermal runaway propagation inhibition system.

The proposed layout is based on the integration of pseudo-passive heat removal and thermal insulation to stop thermal runaway propagation. During the period of thermal runaway propagation inhibition, a portion of heat generation is dissipated from the battery array to the environment through heat removal, and the remainder is addressed by thermal insulation. The proposed system has the advantage of cutting off thermal runaway propagation with relatively small thermal resistance between batteries and is able to be compatible with any type of thermal insulation materials. Furthermore, the proposed layout is passive essentially, so that it can be responded to immediately when thermal runaway propagation happens at the battery array.

2.2. System operation

The pseudo-passive heat removal, comprising of pump-driven cooling unit and thermoelectric modules, is the outstanding characteristic of the proposed system. The pump-driven cooling unit and thermoelectric module serve as the primary and secondary heat removal, respectively. Note that the power of heat removal is provided by thermoelectric modules. In case of system activation, i.e., one of the batteries occurs thermal runaway occasionally, thermoelectric modules convert the battery heat generation to electric energy by the temperature difference between the battery array and the environment to drive the pump-driven cooling unit for the remarkable heat dissipation. Owing to the interaction between the heat generation of the battery array and heat dissipation of the heat removal process, the battery temperature emerges the negative feedback effect, i.e., the heat removal rate is positively related to battery heat generation rate, which is favorable for the cooling of the battery array. The battery temperature comes down gradually and the proposed system shuts down automatically, as the thermal runaway propagation is cut off successfully.

3. System model

The model of the proposed system is composed of a thermal runaway propagation model of the battery array as well as a heat removal model associated with the pump-driven cooling unit and thermoelectric modules. Additionally, the model validation and case study are described as well.

3.1. Thermal runaway propagation model

The thermal runaway propagation model of the battery array is comprised of governing equations, modeling of nail penetration, and boundary conditions. In the thermal runaway propagation model, it is presumed that there is an absence of electrical connectivity between the batteries.

3.1.1. Governing equation

The 3D thermal runaway propagation model of the battery has been built. The temperature distribution is calculated using the following fundamental heat transfer equation [13]:

$$\rho C_{\mathrm{p}} \frac{dT}{dt} = q_{\mathrm{v}} + \frac{\partial}{\partial x}\left(\lambda_{\mathrm{x}} \frac{\partial T}{\partial x}\right) + \frac{\partial}{\partial y}\left(\lambda_{\mathrm{y}} \frac{\partial T}{\partial y}\right) + \frac{\partial}{\partial z}\left(\lambda_{\mathrm{z}} \frac{\partial T}{\partial z}\right) \quad (1)$$

The expression for the volumetric heat generation of battery thermal runaway caused by thermal abuse is as follows [36]:

$$q_{\mathrm{v,\,Bat}} = q_{\mathrm{v,\,JR}} = \frac{1}{V_{\mathrm{JR}}} \cdot H_{\mathrm{TR}} \cdot \frac{\mathrm{d}u}{\mathrm{d}t} \quad (2)$$

H_{TR} encompasses the heat produced by short circuits resulting from separator collapse, as well as the exothermic reactions at elevated temperatures, with its value provided in Ref. [36]:

$$H_{\mathrm{TR}} = \int_{V_{\mathrm{JR}}} \int_{T_1}^{T_3} \rho_{\mathrm{JR}}(T) C_{\mathrm{p,JR}}(T) \cdot dT dV_{\mathrm{JR}} \quad (3)$$

Due to the difficulty in determining the variation of thermophysical parameters during battery thermal runaway, their values are interpolated linearly by the one before and after thermal runaway, as illustrated below [37]:

$$r_i(T)=\begin{cases} r_{i0} & (T<T_2, u>0) \\ r_{i0}-\dfrac{T-T_2}{T_3-T_2}\cdot\Delta r_i & (T_2<T<T_3, u>0) \\ r_{i0}-\Delta r_i & (u=0) \end{cases} \tag{4}$$

where the parameters T_1, T_2, and T_3 are represented by self-generating heat temperature, thermal runaway triggering temperature, and thermal runaway maximum temperature, respectively.

Ref. [37] indicates that when $T>T_2$, the reaction rate remains constant at $Const_{\mathrm{TR}}$, whereas when $T_1<T\leq T_2$, it adheres to the Arrhenius equation. Consequently, the expression for the chemical reaction rate is as follows:

$$\frac{\mathrm{d}u}{\mathrm{d}t}=\begin{cases} A\cdot\exp\left(-\dfrac{E_{\mathrm{a}}}{RT}\right) & (0\leq u\leq 1, T_1<T\leq T_2) \\ Const_{\mathrm{TR}} & (0\leq u\leq 1, T>T_2) \\ 0 & \text{other} \end{cases} \tag{5}$$

3.1.2. Nail penetration model

The origin of thermal runaway propagation, e.g., the initial battery thermal runaway in the battery array, is caused by nail penetration. The volumetric heat generation rate of the battery due to thermal runaway caused by nail penetration is as follows:

$$q_{\mathrm{v,Bat}}=\begin{cases} q_{\mathrm{v,nail}} & (\text{Nail}) \\ q_{\mathrm{v,JR}} & (\text{Jelly Roll}) \end{cases} \tag{6}$$

The power of electrical energy released per unit volume of the nail during the nail penetration process can be expressed as follows [38]:

$$q_{\mathrm{v,nail}}=\frac{1}{V_{\mathrm{nail}}}\cdot H_{\mathrm{nail}}\cdot f(t) \tag{7}$$

where V_{nail} is the volume of the nail inserted into the battery, and $f(t)$ is the function of the energy release rate during the internal short circuit. The released energy reaches its peak at 0.15 s, and the release rate slows down after 0.25 s.

The volumetric heat generation rate of the battery due to thermal runaway caused by nail penetration is as follows:

$$H_{\text{nail}} = \alpha \cdot H_{\text{TR}} \tag{8}$$

where α is the ratio of the heat energy on the nail to the total heat energy. It can be obtained by optimization and parameter identification [37]. α is set to 0.02 in the simulation.

The volumetric heat generation of the jelly roll is as follows:

$$q_{\text{v,JR}} = \frac{1}{V_{\text{JR}}} \cdot H'_{\text{TR}} \cdot \frac{\mathrm{d}u}{\mathrm{d}t} \tag{9}$$

where H'_{TR} refers to the thermal runaway heat generation, accounting for the reduction caused by the short circuit induced by the nail.

3.1.3. Thermal boundary

The geometric model of the battery is composed of four components: the jelly roll, shell, poles, and gas layer. In this model, thermal resistance during heat conduction is simplified into equivalent thermal resistances. The first thermal resistance is the equivalent thermal resistance between the jelly roll and its shell, while the second is the equivalent thermal resistance between the shells of neighboring batteries. The heat transfer equation for these resistances is expressed as follows:

$$-\lambda_{\text{n,f}} \frac{\partial T}{\partial \vec{n}} = \frac{\lambda_{\text{layer}} \left(T_{\text{f}} - T_{\text{b}} \right)}{\delta_{\text{layer}}} \tag{10}$$

In the model, the battery surface is designated as thermally insulated before thermal runaway. After thermal runaway, both convection and radiation heat transfer occur between the cell and its surface. The convection and radiation boundary equations are as follows:

$$-\lambda_{\text{n}} \frac{\partial T}{\partial \vec{n}} = h\left(T - T_{\infty}\right) + \varepsilon\sigma\left(T^4 - T_{\infty}^4\right) \tag{11}$$

3.2. Heat removal model

The pseudo-passive heat removal is by the integration of the pump-driven cooling process and thermoelectric conversion process. Hence, the modeling of the pump-driven cooling unit and thermoelectric modules is described.

3.2.1. Pump-driven cooling unit model

Fig. 2 depicts the pump-driven cooling unit. The pump-driven cooling process model operates under the following assumptions [39]:

(1) The system is thermally insulated from the external environment, with height differences, local resistance, and frictional losses along the path disregarded.

(2) The enthalpy difference of the fluid is negligible within the liquid pump.

(3) The two-phase fluid is in thermodynamic equilibrium and remains homogeneous, with axial heat conduction in both the fluid and the pipe walls being neglected.

(4) The saturation temperature equals the average of the cold source and heat source temperatures, applicable when the charging amount is appropriate [40].

(5) During stable operation, a gas-liquid interface exists within the reservoir.

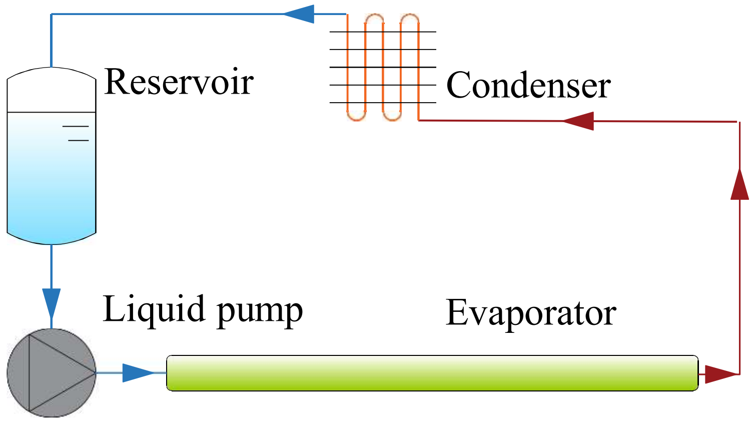

Fig. 2. Pump-driven cooling cycle.

According to the conservation of momentum and energy, the following equations are obtained:

$$m_{\text{in}} = m_{\text{out}} \tag{12}$$

$$Q = m_{\text{out}} h_{\text{out}} - m_{\text{in}} h_{\text{in}} \tag{13}$$

$$Q = kA\Delta T_{\text{m}} \tag{14}$$

$$\Delta T_{\text{m}} = \frac{\Delta T_{\text{t1}} - \Delta T_{\text{t2}}}{\ln \dfrac{\Delta T_{\text{t1}}}{\Delta T_{\text{t2}}}} \tag{15}$$

The relationship of pump power, pressure drop, and volumetric flow rate is fitted using concurrent experimental data from Ref. [41], resulting in a calculation with acceptable accuracy (The corresponding errors can be seen in Fig. A. 1 in the appendix.), as shown below:

$$P_{\mathrm{C,p}} = 7.76\Delta p^{0.0214} q_{\mathrm{v}}^{0.622} \tag{16}$$

The equation governing the fan speed of the condenser and the cold side of the thermoelectric module in relation to input power is as follows [42]:

$$v = \left(\frac{P}{P_{\mathrm{r}}}\right)^{\frac{1}{3}} v_{\mathrm{r}} \tag{17}$$

The working fluid inside the evaporator can be categorized into three regions: subcooled, two-phase, and superheated [43]. In the condenser, the condensation process is divided into the two-phase region and the subcooled region, aligned according to the direction of the working fluid's flow [43]. For heat transfer calculations, the Gnielinski correlation [44] is employed for single-phase turbulent flow, the Gungor-Winterton correlation [45] is used for two-phase evaporation, and the Shah correlation [46] is applied for two-phase condensation. For flow resistance calculations, 64/Re is used for single-phase laminar pressure drop calculations, the Blasius formula [47] is utilized for single-phase turbulent flow, and the Friedel formula [48] is applied for two-phase fluid.

The energy efficiency ratio of the pump-driven cooling process, *EER*, is as follows [41]:

$$EER = \frac{Q_{\mathrm{rem}}}{P_{\mathrm{total}}} \tag{18}$$

where P_{total} is the total power consumption of the liquid pump and fans.

3.2.2. Thermoelectric conversion process model

The thermoelectric component establishes an overall thermal equilibrium, making the following assumptions [49]:

(1) The Joule effect is symmetrically distributed between the hot and cold junctions;

(2) The Seebeck coefficient, thermal conductivity, and electrical conductivity of the thermoelectric material are constant, derived from the average temperature of the hot and cold junctions.

These assumptions apply to steady-state heat transfer not dominated by the Joule effect. Given the aforementioned assumptions and the energy conservation equation, the thermal flux at the hot and cold junctions of the thermoelectric leg can be calculated using the following formula [50]:

$$Q_{\mathrm{H}} = \bar{\alpha} \cdot I \cdot T_{\mathrm{H}} + \bar{k} \cdot \Delta T - \frac{1}{2} \cdot \bar{R} \cdot I^2 \tag{19}$$

$$Q_{\mathrm{C}} = \bar{\alpha} \cdot I \cdot T_{\mathrm{C}} + \bar{k} \cdot \Delta T + \frac{1}{2} \cdot \bar{R} \cdot I^2 \tag{20}$$

The total output power of the thermoelectric module is calculated as follows [51]:

$$P_{\mathrm{out}} = \sum [\alpha_{\mathrm{TE}} I \left(T_{\mathrm{H},i} - T_{\mathrm{C},i}\right) - I^2 R_{\mathrm{TE}}] \tag{21}$$

In the thermoelectric module, the formula for calculating thermoelectric conversion efficiency is [49]:

$$\eta = \frac{P}{Q_{\mathrm{H}}} \tag{22}$$

Additionally, the thermal resistance of the thermocouple has been simplified to a network that includes the thermal resistances of the ceramic substrate, copper substrate, solder, P-type semiconductor, and N-type semiconductor.

3.3. Model validation

The model-solving method and validation are described in detail.

3.3.1. Model solving

Fig. 3 presents the simulation framework. The thermal runaway propagation model is implemented in Ansys Fluent®, while the thermoelectric conversion model and the pump-driven cooling model are executed in Python™. The PyFluent module is utilized to invoke the Fluent solver within Python. At the beginning of the computation, initial parameters are provided. The thermal runaway propagation model calculates the temperature field of the battery array, which is then conveyed to both the thermoelectric conversion model and the pump-driven cooling model. These models independently compute their parameters and return the thermal boundary conditions to the battery array. The iterative calculation of the pump-driven cooling model takes the pump speed as the iteration variable, with the total pressure drop serving as the criterion for the end of the iteration. Furthermore, the thermoelectric conversion model also relays electric energy parameters to the pump-driven cooling model. When it comes to the thermal calculation of the evaporator, distinct correlations will be employed for different flow regions within the respective segments.

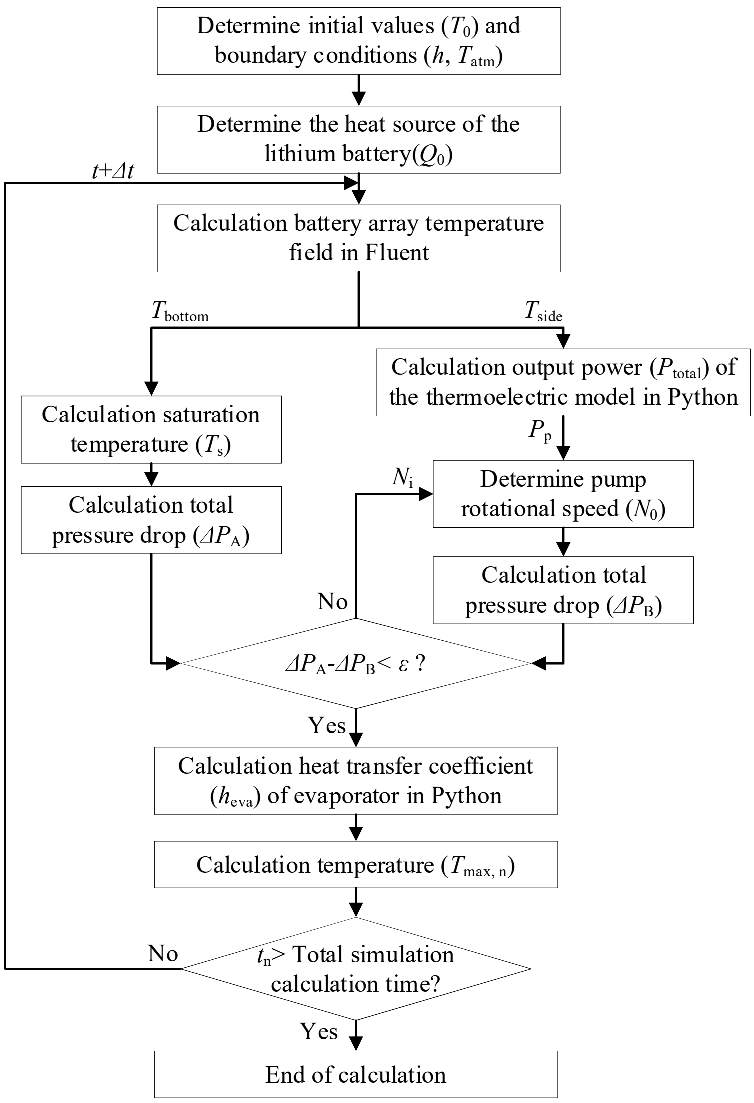

Fig. 3. Calculation framework of numerical simulation.

The thermal runaway model is validated for grid count and time step. Fig. 4(a) illustrates the temperature of the jelly roll for different grip numbers. The model employed grid counts of 5.2×10^5, 1.05×10^6, and 2.10×10^6, and the simulation results are compared. It displays that the deviation of jelly roll temperature is 2.6% when the grid number goes up from 5.2×10^5 to 2.10×10^6; however, the computational time rises remarkably. Thereby, the grid number of 5.2×10^5 is used in the simulation, for the tradeoff of accuracy and efficiency.

Fig. 4(b) illustrates the temperature of the jelly roll at various time steps, with calculations performed for time steps of 0.1 s, 0.01 s, and 0.001 s. The simulation reveals that the maximum deviation in peak temperature is 1.11%, and the maximum deviation in the time to reach peak temperature is 1.08%. Therefore, for the tradeoff of accuracy and efficiency, a time step of 0.1 s can be adopted in subsequent case studies.

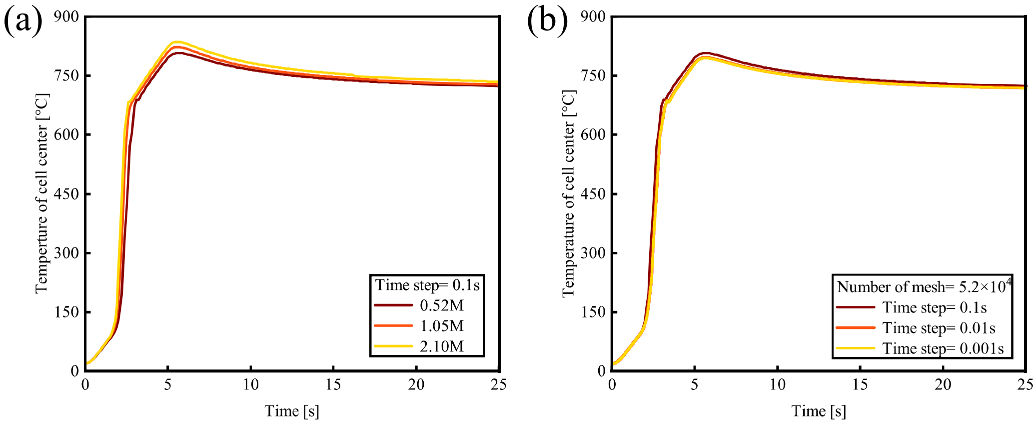

Fig. 4. Independence validation: (a) Grid independence validation, and (b) Step independence validation.

3.3.2. Verification of thermal runaway propagation model

The validation of the thermal runaway propagation model for power batteries is based on the nail penetration thermal runaway propagation experiment detailed in Ref. [37]. A battery array composed of eight 37 Ah lithium-ion batteries arranged in parallel is utilized. It is posited that Bat. 1, located at the edge of the pack, will undergo thermal runaway due to nail penetration, while Bat. 2-Bat. 8 will undergo thermal runaway through heat transfer. Fig. 5 illustrates the jelly roll temperature changes of each battery overtime during the thermal runaway, with dashed lines and solid lines indicating the reference data and the simulation result, respectively. Table 3 shows the relative error of the thermal runaway propagation time, with an average relative error of 7.51%, demonstrating acceptable agreement between the experimental and simulation results.

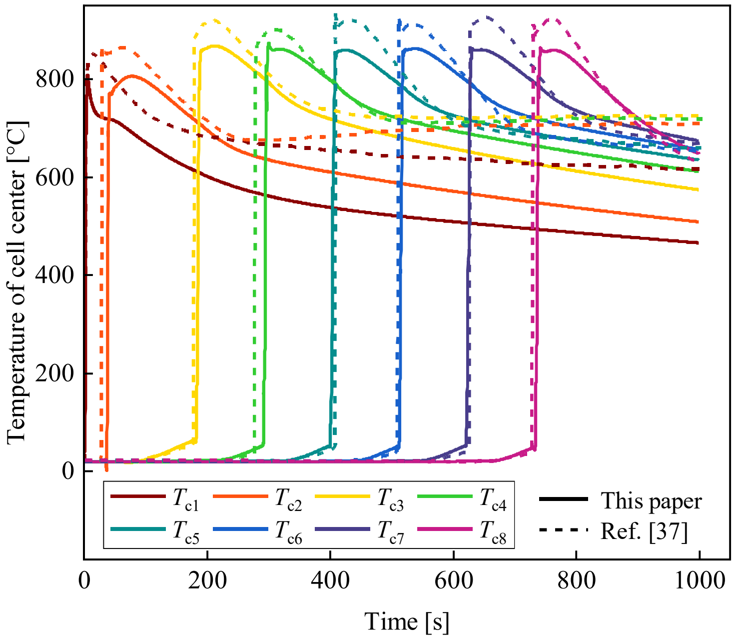

Fig. 5. Comparison of jelly roll temperature.

Table 3

Comparison of the thermal runaway propagation time.

This paper (s)	Ref. [37] (s)	Relative error
29.8	28	6.4%
154	150	2.7%
107.5	99	8.6%
109.3	129	-15.3%
111.1	103	7.9%
109.9	115	-4.4%
111.6	104	7.3%

3.3.3. Verification of pseudo-passive heat removal model

The validation of the pump-driven cooling unit model is based on the operational experiments detailed in Ref. [41]. Fig. 6 presents the phase change temperature and heat flow of the pump-driven cooling system, with solid lines depicting the simulated results and dashed lines reflecting the reference data. In the experiment, the cold source temperature was kept at 18 °C by means of air-conditioner. The phase change temperature exhibits an average deviation of 2.93 °C, while the heat flow shows an average deviation of 15.9%. The discrepancy of simulation and experiment data is acceptable, and is mainly associated with the correlation of pump power (Eq. (16)) as well as the uneven flow during the experiment.

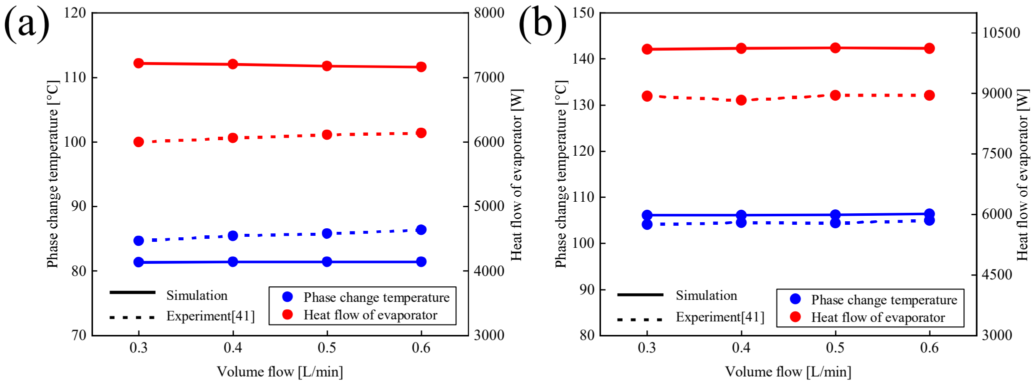

Fig. 6. Comparison of phase change temperature and heat flow of evaporator for the pump-driven cooling unit: (a) Heat source at 150 °C, and (b) Heat source at 200 °C.

Fig. 7 depicts the validation of the thermoelectric module model. In this figure, square dots indicate data from Ref. [52], while solid lines represent the model simulation results. It shows a remarkable consistency between the two sets of data, and the peak discrepancy is 7.37%, implying the accuracy of the thermoelectric module model is satisfactory.

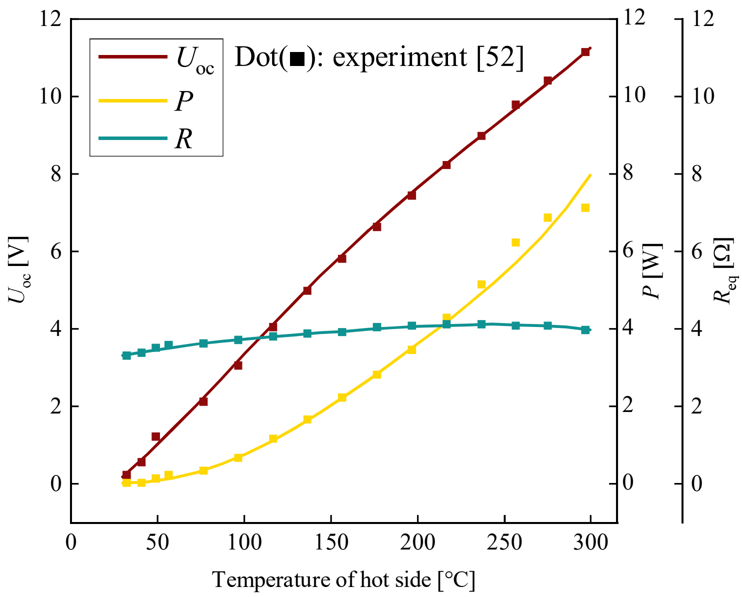

Fig. 7. Validation of the thermoelectric conversion model.

Fig. 8 presents the verification and the deviation of the pseudo-passive heat removal process, e.g., the integration of pump-driven cooling and thermoelectric conversion processes. The model's validation is grounded in the dynamic operation experiments of the heat removal system, as thoroughly described in Ref. [41]. The battery array temperature shows a strong alignment with the experimental data. Due to the thermal inertia of the experimental system, the response to heat is slow, resulting in a relatively large error at the beginning of the simulation. However, as time progresses, the error gradually decreases. After 330 s, the error drops below 10%, and remains below 3% for the majority of the time.

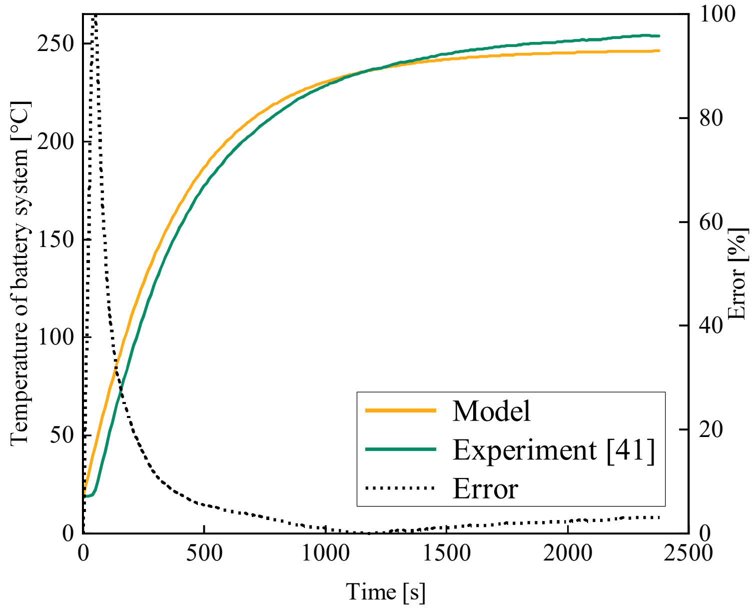

Fig. 8. Validation and deviation of pseudo-passive heat removal model.

3.4. Case study

Fig. 9 depicts the structure of the battery array examined in the case study. This system comprises nine batteries, labeled sequentially from Bat. 1 to Bat. 9. The evaporator is positioned at the base of the battery array, with its flow channels arranged in a serpentine pattern. The flow direction of the working fluid is illustrated by the gray lines in the figure. The heat insulation layer is placed between the z-planes (xOz planes) of the batteries. Due to the smaller heat transfer area, the x-planes (yOz planes) of the cells are not insulated. The thermoelectric module is designed to completely cover the sides of the battery. The total power generated by the thermoelectric module is evenly divided among cold-side radiators, condenser fans, and the water pump. The main parameters of the system components are summarized in Table 4. The composition of the battery encompasses a cathode, an anode, and a shell, with the jelly roll and the gas layer situated above it, all encased within.

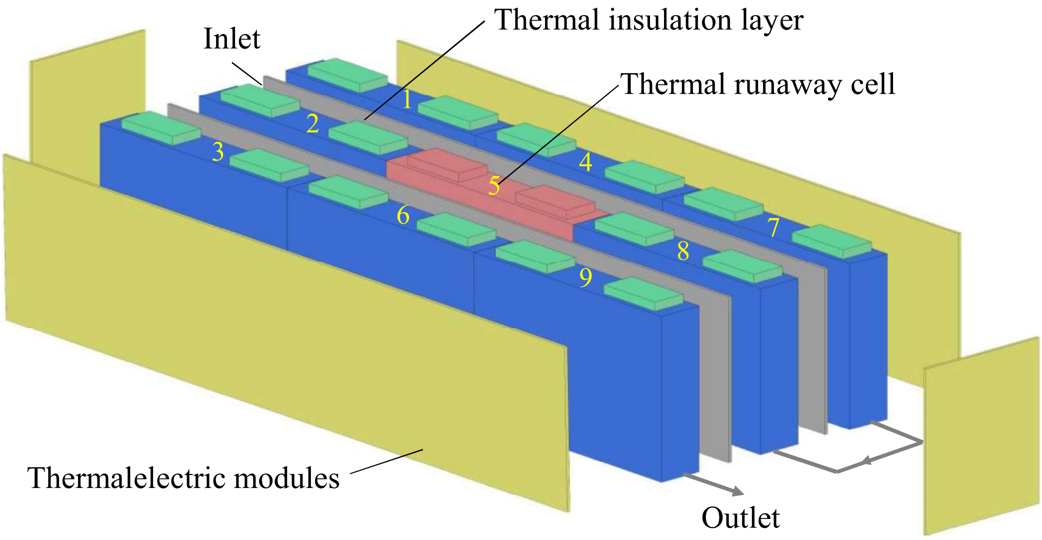

Fig. 9. Structure of battery array.

Table 4

Main parameters used for system simulation.

Parameter	Value
Battery [37]	
Material of cathode/anode	$Li(NiCoMn)_{1/3}O_2$/graphite
Capacity of battery	37 Ah
SOC of battery	100%
Cut-off voltages for charging/discharging	4.2/2.8 V
Weight of battery/mass loss after TR	830/210 g
Dimensions of battery	146×91×26.5 mm
Height of jelly roll/gas layer	80.3/9.3 mm
Thickness of shell/equivalent thermal resistance between shell and jelly roll/equivalent thermal resistance between shell and shell/thermal insulation	0.7/0.4/0.2/0.5 mm
Density of battery	Before TR: 2680 kg/m^3 After TR: 1990.7 kg/m^3
Heat capacity of battery	Before TR: 1100 J/(kg·K) After TR: 788.47 J/(kg·K)
Thermal conductivity in the X direction/ Y direction/ Z direction	Before TR: 15.30/15.3/0.84 W/(m·K) After TR: 8.18/8.18/0.35 W/(m·K)
Heat capacity of equivalent thermal resistance between shell and jelly	1883/66 J/(kg·K)

roll/equivalent thermal resistance between shell and shell	
Thermal conductivity of equivalent thermal resistance between shell and jelly roll/equivalent thermal resistance between shell and shell/thermal insulation	0.22/0.04/0.065 W/(m·K)
Heat transfer coefficient of the top/ side/ bottom	10/8/1 W/(m^2·K)
Temperature of ambiance/self-generating heat/TR triggering/TR maximum	25/105/250/821 °C
Diameter of nail	6 mm
Pre-exponential factor (A)	1.75×10^{12} s^{-1}
Activation energy (E_a)	1.20227×10^{5} J/mol
Pump-driven cooling process model [41]	
Dimensions of evaporator pipe	8×8×1400 mm
Dimensions of condenser pipe	8.52×4500 mm
Area of condenser heat exchange	2.48 m^2
Rib effect coefficient of condenser	18.44
Charge amount of working fluid	0.4
Temperature of ambience	25 °C
Thermoelectric conversion process model [52, 53]	
Installation area of thermoelectric modules	94185 mm^2
Seebeck coefficient of P-type legs	$-1.8027\times10^{-7}T^4+3.2363\times10^{-4}T^3$ $-0.2154T^2+62.9744T-6616.5678\,\mu\text{V/K}$
Seebeck coefficient of N-type legs	$1.8027\times10^{-7}T^4+3.2363\times10^{-4}T^3$ $-0.2154T^2+62.9744T-6616.5678\,\mu\text{V/K}$
Thermal conductivity of P-type legs/N-type legs	$-3.0595\times10^{-9}T^4+4.5678\times10^{-6}T^3$ $-2.5162\times10^{-3}T^2+0.6107T-53.9863\,\text{W/(m}\cdot\text{K)}$
Thermal resistance of copper electrode/solder/hot side ceramic plate/cold side ceramic plate/hot side thermal grease/cold side thermal grease	1.11×10^{-3}/1.99×10^{-3} /0.0207/0.0227/0.0167/0.0184 K/W
Energy distribution of cold-side radiators, condenser fans, and water pump	1:1:1

Note that the thermal runaway of the battery located at the center of the battery array (Bat. 5) is employed to activate the proposed system. For one thing, current battery manufacturing has achieved a safety incident rate of less than 1 in 10^6 batteries produced [54], and most lithium-ion battery incidents stem from thermal runaway in an individual battery [36, 55, 56]. Thus, it is thought that the initial thermal runaway occurs in a single battery. For another thing, it is indicated that batteries undergoing thermal runaway in the center of the battery array are more dangerous than those at the periphery [57]. When thermal runaway occurs in the central battery, less heat is dissipated to the environment and more is transmitted to the neighboring batteries, triggering their thermal runaway easier. Beyond these, the internal power for the proposed system is sourced from the thermoelectric modules located on the sides of the battery array. When thermal runaway occurs in the central battery, the temperature of the outer battery sides remains low, resulting in less power generation. As a result, the heat removal capacity of the pump-driven cooling system is weakened. Therefore, the occurrence of thermal runaway in the central battery represents the most severe operating condition for the proposed system, and corresponding system performances are analyzed and discussed in subsections.

4. Results and discussions

The performance of the proposed system has been analyzed. Additionally, the proposed system has been compared with existing systems.

4.1. Performances of the proposed system

Fig. 10(a) depicts the total and individual thermoelectric heat absorption from each battery. On average, the total thermoelectric heat absorption is 115.66 W, peaking at 139.42 W at 505 s, with an average rate of change of 0.276 W/s. In the early stage of system operation, the battery in the thermal runaway (Bat. 5) generates heat rapidly, causing the side temperature of the battery array as well as the heat absorption rate of the thermoelectric modules to rise quickly. However, at the same time, the heat dissipation in the heat removal process increases due to the internal power improvement, gradually resulting in the peak heat absorption by thermoelectric modules, i.e., the heat removal rate goes up to be the same as battery heat generation one. Fig. 10(b) illustrates the total and individual electrical energy generated by the thermoelectric module at each battery. It is observed that the electrical energy generation follows an initial increase and then gradually declines, reflecting the trend in thermoelectric heat absorption. During the initial phase of system operation, the thermal runaway in Bat. 5 leads to a swift rise in heat generation among the other batteries. As Bat. 5 exhausts its heat release, the heat generation rates of the batteries gradually decrease, driven by the pseudo-passive heat removal process. It is evident that the heat absorbed by the thermoelectric module and the resulting electrical energy output are positively correlated with the heat generation rate of the battery array. The total electrical energy peak is 0.4 W at 459 s, with an average value of 0.30 W. Fig. 10(b) also demonstrates the efficiency of the thermoelectric conversion process. The efficiency is largely determined by the amount of heat absorbed, with its pattern closely reflecting the trend of the electrical energy produced. At 406 s, the thermoelectric conversion efficiency peaks at 0.29%, with an average efficiency of 0.247% over time.

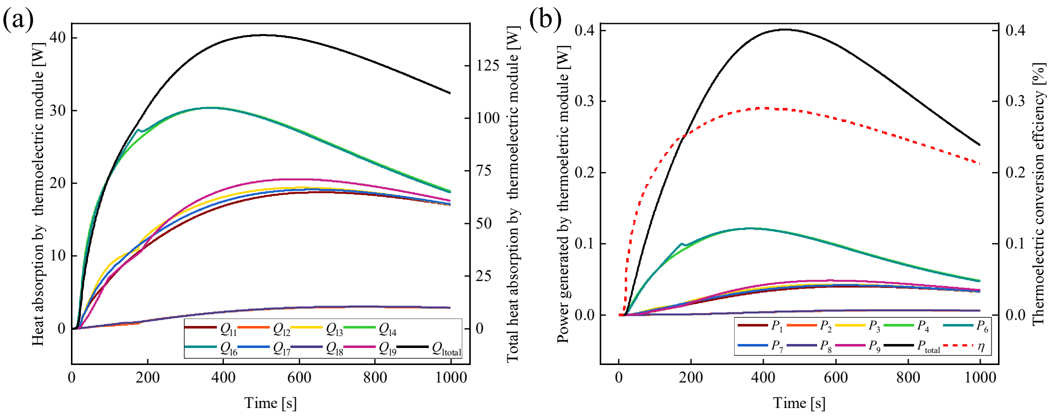

Fig. 10. Thermoelectric conversion process: (a) Total and individual thermoelectric heat absorption from each battery, and (b) Total and individual electric energy generated by the thermoelectric modules at each battery, together with thermoelectric conversion efficiency.

Fig. 11(a) depicts the mass flow rate of the pump-driven cooling process, which initially increases and then gradually decreases over time. This variation is due to the unimodal power generation of the thermoelectric module. As a result, the electric power supplied to the water pump follows the same pattern, causing the pump's flow rate to initially increase and then decrease. The mass flow rate attains its maximum value of 0.41 g/s at 460 s, while the average value is 0.28 g/s. The evaporator outlet vapor quality of working fluid initially diminishes over time before a slight increase. The variation of vapor quality is roughly controlled through the working fluid flow rate, i.e., the more the flow rate is, the less the vapor quality becomes. By 600 s, the reduction in flow rate reaches its peak, and the pump-driven cooling power also diminishes, leading to only a minor increase in vapor quality. Fig. 11(b) illustrates the allocation of vapor quality along the flow direction at 600 s, revealing that the peak vapor quality at the evaporator outlet is approximately 0.2 during the operational period. In traditional pump-driven cooling units, the flow rate remains relatively stable, and the cooling capacity generally has a negative correlation with the quality, while the heat generation of the heat source remains constant. As a result, the evaporator quality nearly keeps fixed over time. In contrast, for the proposed system, the flow rate initially increases and then decreases due to the influence of the thermoelectric module's power output. Moreover, the heat generation and temperature of the heat source fluctuate significantly over time, leading to unstable cooling capacity. Therefore, the relationship between quality and cooling capacity differs from that of the traditional system. In addition, as the exothermic reactions of battery thermal runaway essentially cease within 20 s—distinct from the steady heat sources and abundant flow rates characteristic and abundant flow rates characteristic of conventional systems—the proposed pump-driven cooling unit presents a slightly lower vapor quality at the evaporator outlet than that of traditional systems.

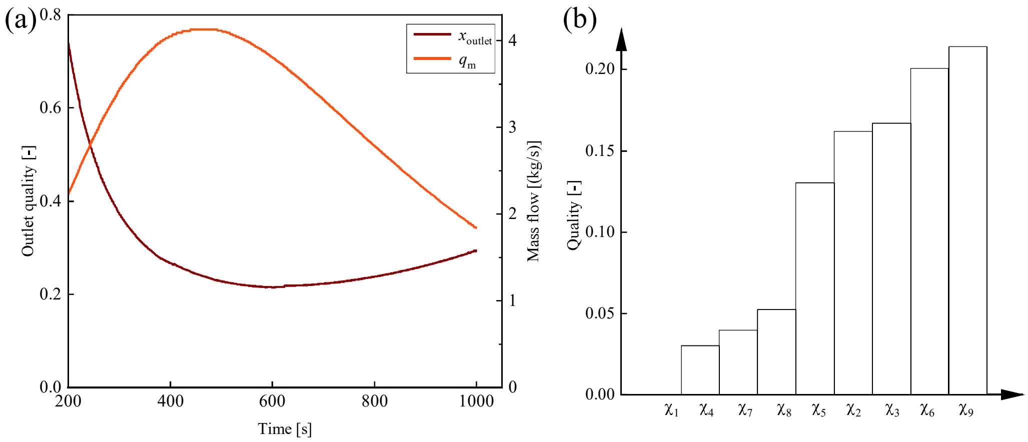

Fig. 11. Quality and mass flow of the pump-driven cooling process: (a) Quality at evaporator outlet and mass flow, and (b) Quality allocation along the flow direction at 600 s.

Fig. 12(a) presents the overall and individual pump-driven cooling power for each battery. Solid lines represent the cooling power for each battery, while the dashed line indicates the total cooling power. Cooling power for the Bat. 4, Bat. 5, and Bat. 6 exhibit an initial increase followed by a decrease. This is because Bat. 5, being the thermal runaway battery, generates the most heat. Bat. 4 and Bat. 6, having the largest contact area with Bat. 5, receive the most heat transfer. For other batteries, their heat dissipation is relatively minor due to the less heat generation. The total pump-driven cooling power, the sum of the individual cooling power, initially increases and then decreases. The average total pump-driven cooling power is 209.92 W within 1000 s, peaking at 460.65 W at 181 s. The average change rate of heat dissipation for the pump-driven cooling process is 2.55 W/s from 0 to 181 s and -0.40 W/s from 181 to 1000 s. Fig. 12(b) illustrates the energy efficiency ratio of the pump-driven cooling process. Initially, there is a rapid decline in efficiency, which later stabilizes. This trend occurs because the reduction in pump-driven cooling power gradually slows down, while the electric power generated by thermoelectric conversion initially rises before falling. Thus, their ratio undergoes this variation. The time-averaged *EER* is 622.49, eventually stabilizing around 520.

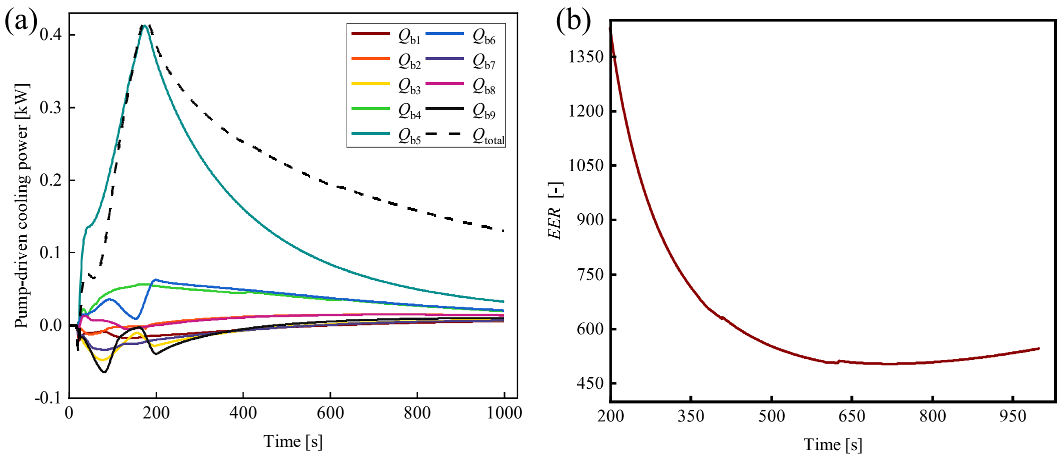

Fig. 12. Cooling capacity and *EER* of the pump-driven cooling process: (a) Total and individual pump-driven cooling power, and (b) *EER*.

Fig. 13(a) illustrates the ratios of heat removal from the system. η_c is the ratio of pump-driven cooling power to the heat generated by the battery array, and η_{TEG} is the ratio of heat absorption by thermoelectric conversion to the same. The dashed line represents the total ratio of heat removal, which is the sum of both. The ratio of pump-driven cooling power to the heat generated by the battery array, the ratio of heat absorption by thermoelectric conversion to the battery array, and the total ratio of heat removal increase progressively over time, reaching final values of 30.9%, 17.0%, and 47.9%, respectively, with average values over time being 16.8%, 7.8%, and 24.6%. This indicates that heat is primarily managed through the thermal insulation approach during the initial phase of thermal runaway. As the temperature of the battery array goes up, the heat dissipation by the pseudo-passive heat removal is enhanced simultaneously and plays an important role in the thermal runaway propagation inhibition. Fig. 13(b) depicts the temperature of the jelly roll in the critical battery. Thermal runaway occurs in Bat. 5. Bat. 2, Bat. 4, Bat. 6, and Bat. 8, which are in direct contact with Bat. 5, are designated as critical batteries. When heat transfer triggers battery thermal runaway, it will first occur in these batteries. Bat. 4 and Bat. 6, which have the same contact area with Bat. 5, reach a peak temperature of 224 °C at 102 s, while Bat. 2 and Bat. 8 peaked at 204.8 °C at 52 s. Obviously, they do not reach the thermal runaway triggering temperature of 250 °C, thereby thermal runaway propagation is inhibited successfully. The proposed system introduces heat removal based on pump-driven cooling, where the large heat transfer coefficient significantly reduces reliance on thermal insulation. Thus, under conditions of lower thermal resistance, the thermal runaway propagation can be effectively inhibited. Specifically, a thermal insulation layer with a resistance of 0.00769 ($m^2 \cdot K$)/W is applied only on the z-plane, while no insulation is applied on the x-plane.

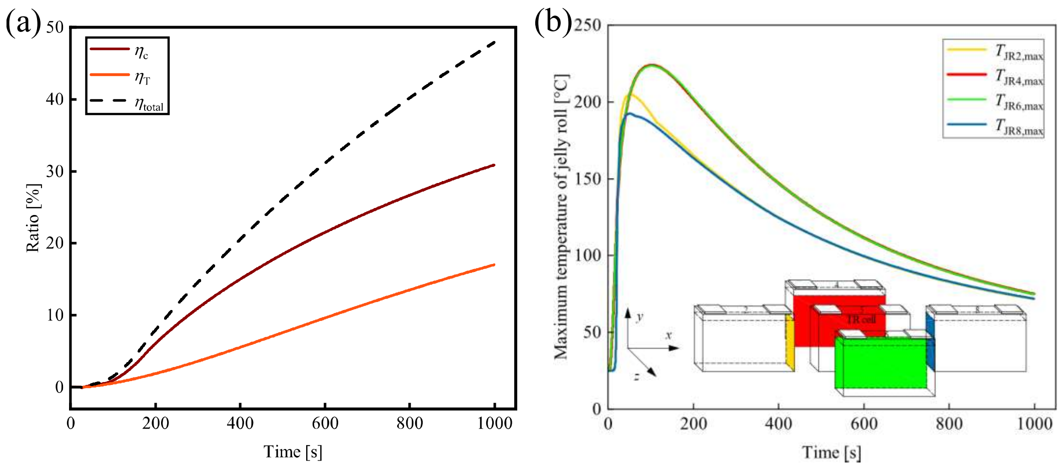

Fig. 13. Thermal runaway propagation inhibition process: (a) Ratios of heat removal from the system, and (b) Temperature of the jelly roll in the critical battery.

4.2. Comparison of the proposed and existing system

The comparison of thermal resistance and heat transfer coefficient between the proposed system and existing systems is presented in Table 5. Considering Ref. [28, 29, 31, 33, 58], all the reviewed solutions utilize a hybrid solution that combines thermal insulation with heat removal, employing single-phase liquid cooling. These systems typically achieve heat transfer coefficients between 5 and 160 W/(m^2·K), with thermal insulation resistance ranging from 0.015 to 0.05 (m^2·K)/W. In contrast, the proposed system boasts an overall heat transfer coefficient of 687.1 W/(m^2·K) (The average heat transfer coefficients of the pump-driven cooling process is displayed in Table 6), far surpassing those of the existing solutions due to the phase-change heat transfer of the pump-driven cooling process, while its thermal resistance necessary to stop the thermal runaway is consequently lower at 0.00769 (m^2·K)/W. Additionally, the thermal insulation layers are positioned solely on the z-plane, leaving the x-plane completely uninsulated. Focusing specifically on Ref. [33] and Ref. [18], along with the proposed system, all aim to inhibit thermal runaway propagation in 37 Ah prismatic lithium-ion batteries. The system described in Ref. [33] has a total heat transfer coefficient of 75 W/(m^2·K) and a thermal resistance of 0.01538 (m^2·K)/W. The proposed system, however, achieves an 816% increase in heat transfer coefficient and a 50.01% reduction in thermal resistance compared to this. Similarly, the thermal resistance in Ref. [18] reaches 0.050 (m^2·K)/W, which the proposed system reduces by an impressive 84.62%. Therefore, it is clear that the proposed system can effectively inhibit thermal runaway propagation under lower thermal resistance. Notably, while the previously mentioned solutions rely on external power sources, the proposed system functions autonomously, without the need for external power, thereby providing reliability and superior safety in extreme conditions.

Table 5

Comparison of thermal resistance and heat transfer coefficient.

No.	C (Ah)	R [W/(m^2·K)]	Variation of R	h [W/(m^2·K)]	Variation of h
This paper	37	0.00769	/	687.1	/
1 [31]	10	0.03846	-80.01%	490	+40.2%
2 [58]	20	0.05	-84.62%	None	/
3 [28]	25	0.015	-48.73%	None	/
4 [18]	37	0.05	-80.01%	None	/
5 [33]	37	0.01538	-50.02%	75	+816%

Table 6

Time-averaged value of the heat transfer coefficient.

h_1	h_2	h_3	h_4	h_5	h_6	h_7	h_8	h_9	h_{total}

443.4	718.3	703.4	730.5	867.4	845.4	508.0	642.6	725.3	687.1

The comparison of pump-driven cooling unit performances between the proposed system and the existing one is presented in The proposed system exhibits a thermal flux that is comparable to or slightly lower than that of the conventional pump-driven cooling system. This is attributed to the characteristic nature of heat generation during the battery thermal runaway process, which initially escalates sharply and subsequently declines, leading to a reduced thermal flux in the later stages and thereby lowering the overall thermal output. The heat transfer coefficient is likewise comparable or marginally diminished. In the evaporator, the heat transfer process can be regarded as flow boiling, involving both boiling and thermal convection contributions [61]. The lower heat transfer coefficient is attributed to the fact that, during the heat exchange process in the proposed system, the quality is relatively low, with the contribution from phase-change heat transfer being large but proportionally small, while the contribution from forced convection heat transfer is small but proportionally high. The notably elevated *EER* of the proposed system is primarily due to differences in working fluids. For instance, while R22 is used as the refrigerant in Ref. [59], the proposed system employs water. At 25 °C, the latent heat of vaporization for R22 is 182.7 kJ/kg, whereas for water it is 2441.7 kJ/kg—13.4 times greater. This substantial difference results in a significantly lower required flow rate to absorb the same amount of heat. Although water has a higher viscosity than R22, the influence of flow rate is more pronounced. Consequently, the overall pump power is considerably reduced, leading to a markedly higher *EER*.

Table 7. Considering Ref. [40, 59, 60], which discuss the application of pump-driven cooling in data centers, aerospace components, and heating ventilating and air conditioning. The proposed system exhibits a thermal flux that is comparable to or slightly lower than that of the conventional pump-driven cooling system. This is attributed to the characteristic nature of heat generation during the battery thermal runaway process, which initially escalates sharply and subsequently declines, leading to a reduced thermal flux in the later stages and thereby lowering the overall thermal output. The heat transfer coefficient is likewise comparable or marginally diminished. In the evaporator, the heat transfer process can be regarded as flow boiling, involving both boiling and thermal convection contributions [61]. The lower heat transfer coefficient is attributed to the fact that, during the heat exchange process in the proposed

system, the quality is relatively low, with the contribution from phase-change heat transfer being large but proportionally small, while the contribution from forced convection heat transfer is small but proportionally high. The notably elevated *EER* of the proposed system is primarily due to differences in working fluids. For instance, while R22 is used as the refrigerant in Ref. [59], the proposed system employs water. At 25 °C, the latent heat of vaporization for R22 is 182.7 kJ/kg, whereas for water it is 2441.7 kJ/kg—13.4 times greater. This substantial difference results in a significantly lower required flow rate to absorb the same amount of heat. Although water has a higher viscosity than R22, the influence of flow rate is more pronounced. Consequently, the overall pump power is considerably reduced, leading to a markedly higher *EER*.

Table 7

Pump-driven cooling unit performance between the proposed system and the existing one.

No.	q (W/m^2)	h [W/(m^2·K)]	*EER*
This paper	6028.55	687.1	622.49
1 [59]	2850.3-3390.7	80-580	10-32.1
2 [60]	4645-23225	700-2500	None
3 [40]	12320	2300-2500	50-120

4.3. Challenge and outlook

One of the primary challenges for the proposed system is the failure of thermoelectric modules. A failure in the thermoelectric module will reduce the system's internal power source, resulting in a decrease in the heat dissipation of the pseudo-passive heat removal process. Experiments show that when the heat absorption of the thermoelectric module drops by 27%, the heat dissipation in the pump-driven cooling process will decrease by 30% [62]. Note that the thermoelectric module is highly reliable, with excellent high-temperature stability and a low probability of failure [63]. Accordingly, the amount of failed thermoelectric modules is not notable, and corresponding impacts on system performances are relatively low. Nevertheless, to ensure system reliability, it is essential to incorporate sufficient margin in the design of the thermal insulation resistance between the batteries.

Another challenge of the proposed system lies in its compatibility with thermal management units. Automotive thermal management systems typically rely on liquid cooling technology. The proposed system is easily compatible with liquid cooling units of which the cooling plate is placed in the bottom of battery array. Two heat exchangers as well as the liquid pump are shared for the proposed system and liquid cooling unit. Only the reservoir, pipelines, and valves are necessary to install additionally. Thermoelectric modules can be installed on the exterior of the battery array. Under normal thermal management conditions, the liquid cooling system is activated. During thermal runaway, the thermoelectric module generates power to activate the liquid pump diversion, compressor bypass, and drive the liquid pump and condenser fan, thereby inhibiting the propagation of thermal runaway in the battery array (The integration of the thermal runaway propagation inhibition system with the liquid cooling thermal management system can be seen in Fig. A. 2 in the appendix.). In this regard, the cooling plate (evaporator of the pump-driven cooling unit) and radiator of the liquid cooling unit (condenser of the pump-driven cooling unit) are essential to design properly through the comprehensive consideration of thermal management as well as thermal runaway propagation inhibition.

5. Conclusions

This article proposes a pseudo-passive power battery thermal runaway propagation inhibition system, aiming at reducing the thermal resistance necessary to block the thermal runaway and being independent of external power sources. A comprehensive model of the system's operational process was developed, followed by an in-depth performance analysis using a 3×3 battery array. The main conclusions of this study are as follows:

(1) The model of the proposed system is built by the lumped parameter model of pump-driven cooling and thermoelectric conversion processes as well as a 3D model of thermal runaway propagation. The lumped parameter model and 3D model are solved in Python™ and Ansys Fluent®, respectively. The PyFluent module is utilized to invoke the Fluent solver within Python. The model of the proposed system is verified by existing simulations and experiments, and the average deviation is 6.91%.

(2) The pseudo-passive heat removal process, integrating with pump-driven cooling and thermoelectric conversion processes, addresses 24.6% of the battery heat generation, with 16.8% managed by the pump-driven cooling process and 7.76% by the thermoelectric conversion process. Furthermore, the mean heat transfer

coefficient of pseudo-passive is 687.1 W/(m^2·K), mitigating the dependence of thermal runaway propagation inhibition on thermal insulation. A thermal insulation layer with a resistance of 0.00769 (m^2·K)/W is applied only to the z-plane of the battery, leaving the x-plane without insulation, indicating that the thermal insulation essential to block the thermal runaway propagation is 48-85% lower than the existing system.

Acknowledgments

This work is supported by: (1) National Natural Science Foundation of China under the contract No. 52376009, (2) Key Laboratory of Efficient and Clean Energy Utilization of Guangdong Higher Education Institutes under the contract No. KLB10004.

Appendix

The model data for the system pump power shows an 81.82% alignment within a 5% deviation from the experimental results, indicating a good agreement with the experimental data.

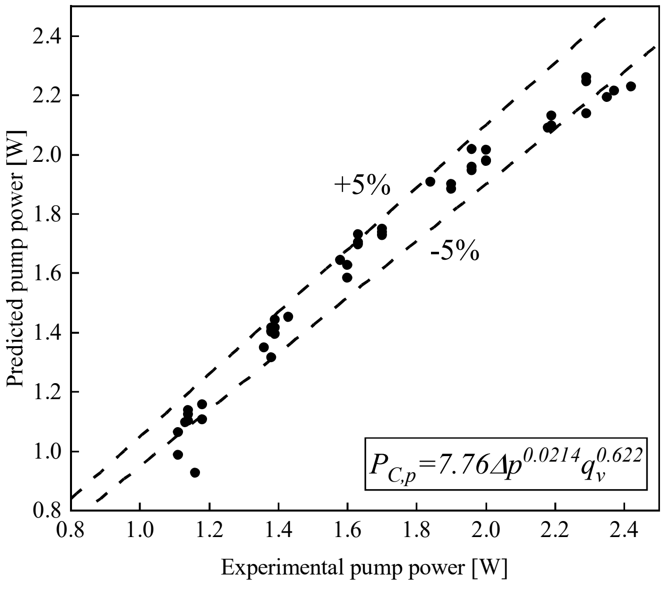

Fig. A. 1. Verification of the pump-driven cooling model's pump power.

The proposed system is easily compatible with liquid cooling units of which the cooling plate is placed in the bottom of battery array.

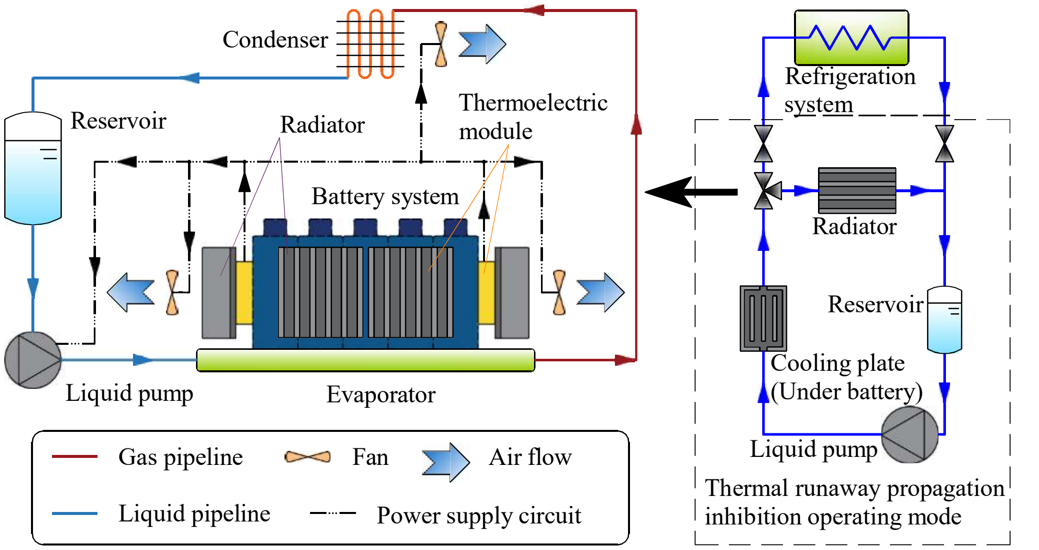

(a) Pseudo-passive power battery thermal runaway propagation inhibition system.

(b) Integration of the proposed system with the liquid cooling system.

Fig. A. 2. Integration of the thermal runaway propagation inhibition system with the liquid cooling thermal management system.

References

[1] IEA. Global ev outlook 2024. (2024). https://www.iea.org/reports/global-ev-outlook-2024

[2] X. Feng, D. Ren, X. He, M. Ouyang, Mitigating thermal runaway of lithium-ion batteries. Joule. 4 (2020) 743-770. https://doi.org/10.1016/j.joule.2020.02.010

[3] X. Feng, M. Ouyang, X. Liu, L. Lu, Y. Xia, X. He, Thermal runaway mechanism of lithium ion battery for electric vehicles: a review. Energy Storage Mater. 10 (2018) 246-267. https://doi.org/10.1016/j.ensm.2017.05.013

[4] H. Wang, Q. Wang, Z. Zhao, C. Jin, C. Xu, W. Huang, Z. Yuan, S. Wang, Y. Li, Y. Zhao, J. Sun, X. Feng, Thermal runaway propagation behavior of the cell-to-pack battery system. J. Energy Chem. 84 (2023) 162-172. https://doi.org/10.1016/j.jechem.2023.05.015

[5] H. Sun, L. Zhang, Q. Duan, S. Wang, S. Sun, J. Sun, Q. Wang, Experimental study on suppressing thermal runaway propagation of lithium-ion batteries in confined space by various fire extinguishing agents. Process Saf. Environ. Protect. 167 (2022) 299-307. https://doi.org/10.1016/j.psep.2022.09.016

[6] S.N. Lauro, J.N. Burrow, C.B. Mullins, Restructuring the lithium-ion battery: a perspective on electrode architectures. eScience. 3 (2023) 100152. https://doi.org/10.1016/j.esci.2023.100152

[7] Y. Yang, W. Yang, H. Yang, H. Zhou, Electrolyte design principles for low-temperature lithium-ion batteries. eScience. 3 (2023) 100170. https://doi.org/10.1016/j.esci.2023.100170

[8] X.L. Chen, Y.D. Gong, X. Li, F. Zhan, X.H. Liu, J.M. Ma, Perspective on low-temperature electrolytes for lifepo4-based lithium-ion batteries. Int. J. Miner. Metall. Mater. 30 (2023) 1-13. https://doi.org/10.1007/s12613-022-2541-1

[9] W.S. Guo, W. Wei, H.W. Zhu, Y.J. Hu, H. Jiang, C.Z. Li, In situ surface engineering enables high interface stability and rapid reaction kinetics for ni-rich cathodes. eScience. 3 (2023). https://doi.org/10.1016/j.esci.2022.10.008

[10] B. Fu, M. Moździerz, A. Kulka, K. Świerczek, Recent progress in ni-rich layered oxides and related cathode materials for li-ion cells. Int. J. Miner. Metall. Mater. 31 (2024) 2345-2367. https://doi.org/10.1007/s12613-024-2948-y

[11] J. Yu, Y. Wei, B. Meng, J. Peng, K. Yang, T. Chen, N. Yang, X. Chuan, Homogeneous distributed natural pyrite-derived composite induced by modified graphite as high-performance lithium-ion batteries anode. Int. J. Miner. Metall. Mater. 30 (2023) 1353-1362. https://doi.org/10.1007/s12613-023-2598-5

[12] K. Wang, D. Ouyang, X. Qian, S. Yuan, C. Chang, J. Zhang, Y. Liu, Early warning method and fire extinguishing technology of lithium-ion battery thermal runaway: a review. Energies. 16 (2023). https://doi.org/10.3390/en16072960

[13] X. Feng, L. Lu, M. Ouyang, J. Li, X. He, A 3d thermal runaway propagation model for a large format lithium ion battery module. Energy. 115 (2016) 194-208. https://doi.org/10.1016/j.energy.2016.08.094

[14] X. Feng, X. He, M. Ouyang, L. Lu, P. Wu, C. Kulp, S. Prasser, Thermal runaway propagation model for designing a safer battery pack with 25ah linixcoymnzo2 large format lithium ion battery. Appl. Energy. 154 (2015) 74-91. https://doi.org/10.1016/j.apenergy.2015.04.118

[15] C. Yuan, Q. Wang, Y. Wang, Y. Zhao, Inhibition effect of different interstitial materials on thermal runaway propagation in the cylindrical lithium-ion battery module. Appl. Therm. Eng. 153 (2019) 39-50. https://doi.org/10.1016/j.applthermaleng.2019.02.127

[16] Q. Li, C. Yang, S. Santhanagopalan, K. Smith, J. Lamb, L.A. Steele, L. Torres-Castro, Numerical investigation of thermal runaway mitigation through a passive thermal management system. J. Power Sources. 429 (2019) 80-88.

https://doi.org/10.1016/j.jpowsour.2019.04.091
[17] L. Torres-Castro, A. Kurzawski, J. Hewson, J. Lamb, Passive mitigation of cascading propagation in multi-cell lithium ion batteries. J. Electrochem. Soc. 167 (2020) 90515. https://doi.org/10.1149/194-7111/ab84fa
[18] X. Yang, Y. Duan, X. Feng, T. Chen, C. Xu, X. Rui, M. Ouyang, L. Lu, X. Han, D. Ren, An experimental study on preventing thermal runaway propagation in lithium-ion battery module using aerogel and liquid cooling plate together. Fire Technol. 56 (2020) 2579-2602. https://doi.org/10.1007/s10694-020-00995-x
[19] J. Weng, D. Ouyang, X. Yang, M. Chen, G. Zhang, J. Wang, Alleviation of thermal runaway propagation in thermal management modules using aerogel felt coupled with flame-retarded phase change material. Energy Conv. Manag. 200 (2019) 112071. https://doi.org/10.1016/j.enconman.2019.112071
[20] R. Kizilel, R. Sabbah, J.R. Selman, S. Al-Hallaj, An alternative cooling system to enhance the safety of li-ion battery packs. J. Power Sources. 194 (2009) 1105-1112. https://doi.org/10.1016/j.jpowsour.2009.06.074
[21] S. Wilke, B. Schweitzer, S. Khateeb, S. Al-Hallaj, Preventing thermal runaway propagation in lithium ion battery packs using a phase change composite material: an experimental study. J. Power Sources. 340 (2017) 51-59. https://doi.org/10.1016/j.jpowsour.2016.11.018
[22] J. Niu, S. Deng, X. Gao, H. Niu, Y. Fang, Z. Zhang, Experimental study on low thermal conductive and flame retardant phase change composite material for mitigating battery thermal runaway propagation. J. Energy Storage. 47 (2022) 103557. https://doi.org/10.1016/j.est.2021.103557
[23] J. Weng, Q. Huang, X. Li, G. Zhang, D. Ouyang, M. Chen, A.C.Y. Yuen, A. Li, E.W.M. Lee, W. Yang, J. Wang, X. Yang, Safety issue on pcm-based battery thermal management: material thermal stability and system hazard mitigation. Energy Storage Mater. 53 (2022) 580-612. https://doi.org/10.1016/j.ensm.2022.09.007
[24] C. Lin, S. Xu, G. Chang, J. Liu, Experiment and simulation of a lifepo4 battery pack with a passive thermal management system using composite phase change material and graphite sheets. J. Power Sources. 275 (2015) 742-749. https://doi.org/10.1016/j.jpowsour.2014.11.068
[25] A.H. Mohammed, R. Esmaeeli, H. Aliniagerdroudbari, M. Alhadri, S.R. Hashemi,

G. Nadkarni, S. Farhad, Dual-purpose cooling plate for thermal management of prismatic lithium-ion batteries during normal operation and thermal runaway. Appl. Therm. Eng. 160 (2019) 114106. https://doi.org/10.1016/j.applthermaleng.2019.114106

[26] J. Xu, C. Lan, Y. Qiao, Y. Ma, Prevent thermal runaway of lithium-ion batteries with minichannel cooling. Appl. Therm. Eng. 110 (2017) 883-890. https://doi.org/10.1016/j.applthermaleng.2016.08.151

[27] H. Fu, J. Wang, L. Li, J. Gong, X. Wang, Numerical study of mini-channel liquid cooling for suppressing thermal runaway propagation in a lithium-ion battery pack. Appl. Therm. Eng. 234 (2023) 121349. https://doi.org/10.1016/j.applthermaleng.2023.121349

[28] W. Zhang, Z. Liang, X. Yin, G. Ling, Avoiding thermal runaway propagation of lithium-ion battery modules by using hybrid phase change material and liquid cooling. Appl. Therm. Eng. 184 (2021) 116380. https://doi.org/10.1016/j.applthermaleng.2020.116380

[29] H. Xu, S. Wu, Y. Chen, W. Luan, Simulation on the management of lithium-ion batteries’ thermal runaway via liquid cooling and phase change barrier. J. Phys. Conf. Ser. 2401 (2022) 12019. https://doi.org/10.1088/1742-6596/2401/1/012019

[30] B. Liu, Y. Su, Q. Deng, S. Jin, Y. Chen, T. Ouyang, Reducing lithium-ion battery thermal runaway risk based on an integrated cooling strategy for electric vehicles. Int. J. Heat Mass Transf. 216 (2023) 124594. https://doi.org/10.1016/j.ijheatmasstransfer.2023.124594

[31] K.S. Kshetrimayum, Y. Yoon, H. Gye, C. Lee, Preventing heat propagation and thermal runaway in electric vehicle battery modules using integrated pcm and micro-channel plate cooling system. Appl. Therm. Eng. 159 (2019) 113797. https://doi.org/10.1016/j.applthermaleng.2019.113797

[32] T. Ouyang, B. Liu, C. Wang, J. Ye, S. Liu, Novel hybrid thermal management system for preventing li-ion battery thermal runaway using nanofluids cooling. Int. J. Heat Mass Transf. 201 (2023) 123652. https://doi.org/10.1016/j.ijheatmasstransfer.2022.123652

[33] X. Rui, X. Feng, H. Wang, H. Yang, Y. Zhang, M. Wan, Y. Wei, M. Ouyang, Synergistic effect of insulation and liquid cooling on mitigating the thermal runaway propagation in lithium-ion battery module. Appl. Therm. Eng. 199 (2021)

117521. https://doi.org/10.1016/j.applthermaleng.2021.117521
[34] Z. Chen, R. Xiong, F. Sun, Research status and analysis for battery safety accidents in electric vehicles. J. Mech. Eng. 24 (2019) 93-104, 116. https://doi.org/10.3901/JME.2019.24.093
[35] S.Q. Zheng, L. Wang, X.N. Feng, X.M. He, Probing the heat sources during thermal runaway process by thermal analysis of different battery chemistries. J. Power Sources. 378 (2018) 527-536. https://doi.org/10.1016/j.jpowsour.2017.12.050
[36] X. Feng, M. Fang, X. He, M. Ouyang, L. Lu, H. Wang, M. Zhang, Thermal runaway features of large format prismatic lithium ion battery using extended volume accelerating rate calorimetry. J. Power Sources. 255 (2014) 294-301. https://doi.org/10.1016/j.jpowsour.2014.01.005
[37] X. Lai, S. Wang, H. Wang, Y. Zheng, X. Feng, Investigation of thermal runaway propagation characteristics of lithium-ion battery modules under different trigger modes. Int. J. Heat Mass Transf. 171 (2021) 121080. https://doi.org/10.1016/j.ijheatmasstransfer.2021.121080
[38] T.G. Zavalis, M. Behm, G. Lindbergh, Investigation of short-circuit scenarios in a lithium-ion battery cell. Electrochem. Soc. 159 (2012) A848. https://doi.org/10.1149/2.096206jes
[39] J. Li, G.P. Peterson, 3d heat transfer analysis in a loop heat pipe evaporator with a fully saturated wick. Int. J. Heat Mass Transf. 54 (2011) 564-574. https://doi.org/10.1016/j.ijheatmasstransfer.2010.09.014
[40] P. Zhang, X. Li, W. Shi, B. Wang, X. Rong, Experimentally comparative study on two-phase natural and pump-driven loop used in hvac systems. Appl. Therm. Eng. 142 (2018) 321-333. https://doi.org/10.1016/j.applthermaleng.2018.07.005
[41] J. Deng, Z. Li, J. Chen, Experiment study of pseudo-passive heat removal system for power battery thermal runaway propagation inhibition. Appl. Therm. Eng. 253 (2024) 123777. https://doi.org/10.1016/j.applthermaleng.2024.123777
[42] A. Kusiak, H. Zheng, Z. Song, On-line monitoring of power curves. Renew. Energy. 34 (2009) 1487-1493. https://doi.org/10.1016/j.renene.2008.10.022
[43] S. Zhang, G. Ma, F. Zhou, Experimental study on a pump driven loop-heat pipe for data center cooling. J. Energy Eng. 141 (2015) 4014054. https://doi.org/10.1061/(ASCE)EY.1943-7897.0000253

[44] V. Gnielinski, New equations for heat and mass transfer in turbulent pipe and channel flow. International chemical engineering. 16 (1976) 359-367.

[45] H. Wang, S. Touber, Distributed and non-steady-state modelling of an air cooler. Int. J. Refrig. 14 (1991) 98-111. https://doi.org/10.1016/0140-7007(91)90082-R

[46] M.M. Shah, Comprehensive correlations for heat transfer during condensation in conventional and mini/micro channels in all orientations. Int. J. Refrig. 67 (2016) 22-41. https://doi.org/10.1016/j.ijrefrig.2016.03.014

[47] H. Blasius, Das aehnlichkeitsgesetz bei reibungsvorgängen in flüssigkeiten., Springer Berlin Heidelberg, Berlin, 1913.

[48] F. Vera-García, J.R. García-Cascales, J.M. Corberán-Salvador, J. Gonzálvez-Maciá, D. Fuentes-Díaz, Assessment of condensation heat transfer correlations in the modelling of fin and tube heat exchangers. Int. J. Refrig. 30 (2007) 1018-1028. https://doi.org/10.1016/j.ijrefrig.2007.01.005

[49] G. Fraisse, J. Ramousse, D. Sgorlon, C. Goupil, Comparison of different modeling approaches for thermoelectric elements. Energy Conv. Manag. 65 (2013) 351-356. https://doi.org/10.1016/j.enconman.2012.08.022

[50] A. Montecucco, J.R. Buckle, A.R. Knox, Solution to the 1-d unsteady heat conduction equation with internal joule heat generation for thermoelectric devices. Appl. Therm. Eng. 35 (2012) 177-184. https://doi.org/10.1016/j.applthermaleng.2011.10.026

[51] X. Lu, X. Yu, Z. Qu, Q. Wang, T. Ma, Experimental investigation on thermoelectric generator with non-uniform hot-side heat exchanger for waste heat recovery. Energy Conv. Manag. 150 (2017) 403-414. https://doi.org/10.1016/j.enconman.2017.08.030

[52] D. Luo, R. Wang, Experimental test and estimation of the equivalent thermoelectric properties for a thermoelectric module. J. Energ. Resour. Technol. 143 (2021). https://doi.org/10.1115/1.4050132

[53] C. Hsu, G. Huang, H. Chu, B. Yu, D. Yao, An effective seebeck coefficient obtained by experimental results of a thermoelectric generator module. Appl. Energy. 88 (2011) 5173-5179. https://doi.org/10.1016/j.apenergy.2011.07.033

[54] G.G. Eshetu, S. Grugeon, S. Laruelle, S. Boyanov, A. Lecocq, J.P. Bertrand, G. Marlair, In-depth safety-focused analysis of solvents used in electrolytes for large scale lithium ion batteries. Phys. Chem. Chem. Phys. 15 (2013) 9145-9155.

https://doi.org/10.1039/c3cp51315g

[55] D. Ren, X. Feng, L. Lu, M. Ouyang, S. Zheng, J. Li, X. He, An electrochemical-thermal coupled overcharge-to-thermal-runaway model for lithium ion battery. J. Power Sources. 364 (2017) 328-340. https://doi.org/10.1016/j.jpowsour.2017.08.035

[56] X. Feng, J. Sun, M. Ouyang, F. Wang, X. He, L. Lu, H. Peng, Characterization of penetration induced thermal runaway propagation process within a large format lithium ion battery module. J. Power Sources. 275 (2015) 261-273. https://doi.org/10.1016/j.jpowsour.2014.11.017

[57] Z.Y. Jiang, Z.G. Qu, J.F. Zhang, Z.H. Rao, Rapid prediction method for thermal runaway propagation in battery pack based on lumped thermal resistance network and electric circuit analogy. Appl. Energy. 268 (2020) 115007. https://doi.org/10.1016/j.apenergy.2020.115007

[58] X. Liu, Z. Zhou, W. Wu, J. Lv, C. Hu, L. Gao, Y. Li, Y. Li, Y. Song, Inhibition of thermal runaway propagation in lithium‐ion battery pack by minichannel cold plates and insulation layers. Int. J. Energy Res. 2023 (2023) 6661693. https://doi.org/10.1155/2023/6661693

[59] Y. Ma, G. Ma, S. Zhang, F. Zhou, Cooling performance of a pump-driven two phase cooling system for free cooling in data centers. Appl. Therm. Eng. 95 (2016) 143-149. https://doi.org/10.1016/j.applthermaleng.2015.11.002

[60] P. Zhang, K. Liu, Y. Li, X. Yang, X. Li, Experimental research on dynamic characteristics and control strategy of the pump-driven two-phase loop with dual evaporators. Case Stud. Therm. Eng. 38 (2022) 102327. https://doi.org/10.1016/j.csite.2022.102327

[61] R. Khodabandeh, Heat transfer in the evaporator of an advanced two-phase thermosyphon loop. Int. J. Refrig. 28 (2005) 190-202. https://doi.org/10.1016/j.ijrefrig.2004.10.006

[62] J. DENG, Z. LI, J. CHEN, Pseudo-passive heat removal system for thermal safety of power battery. CIESC J. 74 (2024) 4679-4687. https://doi.org/10.11949/0438-1157.20230786

[63] G. Wu, Q. Zhang, X.J. Tan, Y.T. Fu, Z. Guo, Z.W. Zhang, Q.Q. Sun, Y. Liu, H.L. Shi, J.S. Li, J.G. Noudem, J.H. Wu, G.Q. Liu, P. Sun, H.Y. Hu, J. Jiang, Bi2te3-based thermoelectric modules for efficient and reliable low-grade heat recovery.

Adv. Mater. 36 (2024). https://doi.org/10.1002/adma.202400285